Electronic Supplementary Information (ESI) of

Synergistic design of a new PbHfO$_3$-based antiferroelectric solid solution with high

energy storage and large strain performances under low electric fields

Hongyan Wan[a,b], Zenghui Liu[a*], Fangping Zhuo[c] Jingwen Xi[b,d], Pan Gao[e], Kun Zheng[a], Luyue Jiang[a],

Jun Xu[a], Jingrui Li[a], Jie Zhang[a], Jian Zhuang[a], Gang Niu[a], Nan Zhang[a], Wei Ren[a], and Zuo-Guang Ye[b*]

[a] Electronic Materials Research Laboratory, Key Laboratory of the Ministry of Education & International

Center for Dielectric Research, School of Electronic and Information Engineering, Xi'an Jiaotong

University, Xi'an 710049, China

[b] Department of Chemistry and 4D LABS, Simon Fraser University, Burnaby, British Columbia V5A

1S6, Canada

[c] Department of Materials and Earth Sciences, Technical University of Darmstadt, 64287 Darmstadt,

Germany

[d] College of Material Science and Engineering, Sichuan University, Chengdu 610065, China

[e] School of Electronic Information & Artificial Intelligence, Shaanxi University of Science and

Technology, Xi'an, 710021, China

*Corresponding authors

Zenghui Liu, Email: liu.z.h@xjtu.edu.cn

Zuo-Guang Ye, Email: zye@sfu.ca

In order to suppress the formation of the secondary phases $PbWO_4$ and Pb_2WO_5, as well as the pyrochlore phase in the final product, the $ZnWO_4$ precursor phase needs to be first synthesized. **Fig. S1** shows the XRD pattern of the as-prepared $ZnWO_4$ precursor, exhibiting excellent agreement between the diffraction peaks of PDF # 15-0774 of $ZnWO_4$. This confirms the successful formation of the $ZnWO_4$ precursor phase.
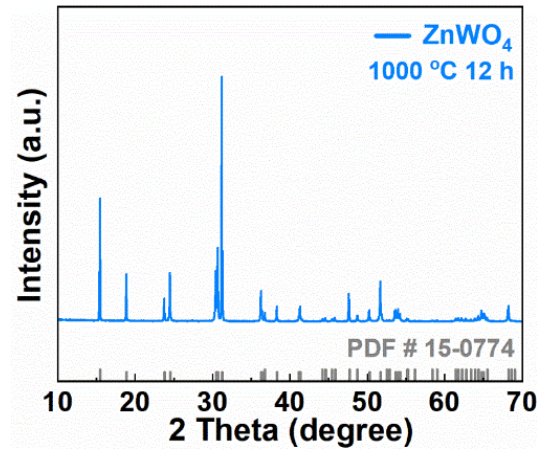

Fig. S1. XRD result of the B-site precursor $ZnWO_4$. The pattern agrees well with the PDF # 15-0774 of $ZnWO_4$.

The orthorhombic *Pbam* $\sqrt{2}a \times 2\sqrt{2}a \times 2a$ lattice is converted into the pseudocubic $a_{pc} \times a_{pc} \times a_{pc}$ lattice setting (a_{pc} = cell dimension of PE$_C$ phase) by the following matrix:

$$(h_o \ k_o \ l_o)\begin{pmatrix} 1/2 & -1/2 & 0 \\ 1/4 & 1/4 & 0 \\ 0 & 0 & 1/2 \end{pmatrix} = (h_{pc} \ k_{pc} \ l_{pc}) \tag{S1}$$

It is observed from **Fig. S2** that a PbO_2-typed secondary phase marked by black solid circles appears when the concentration of PZnW reaches 0.25, indicating that the solubility limit is achieved.

Table S1. Refined crystal structural parameters for the (1-x)PHf-xPZnW ceramics

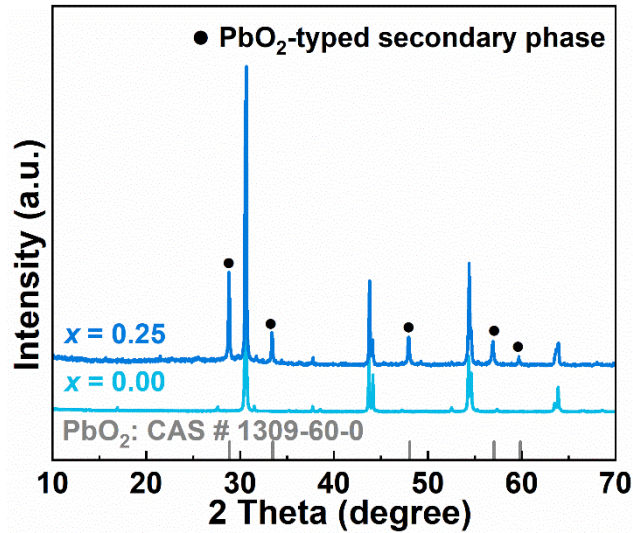| Composition	Space	Lattice parameters				R-factors		
x	group	a (Å)	b (Å)	c (Å)	V (Å^3)	R_{wp} (%)	R_{exp} (%)	R_p (%)
0.00	*Pbam*	5.84782	11.71431	8.19732	561.5425	11.631	4.335	9.347
0.05	*Pbam*	5.84481	11.70888	8.19764	561.0152	11.914	4.250	9.356
0.10	*Pbam*	5.84523	11.70771	8.19683	560.9440	13.325	4.531	10.482
0.15	*Pbam*	5.84481	11.70616	8.19698	560.8397	12.589	4.435	9.767
0.20	*Pbam*	5.84460	11.70711	8.19783	560.9251	11.637	4.416	9.038

Fig. S2. Room temperature XRD patterns of the (1-x)PHf-xPZnW (x = 0.00 and 0.25) ceramics.

Fig. S3-A(a) - (e) illustrates the surface morphology of the (1-x)PHf-xPZnW ceramics with various compositions. The pure PHf ceramics display smaller grain sizes and some pores. The partial substitution of PZnW for PHf results in a significant increase in the average grain size and a reduction in porosity, leading to a denser microstructure. Similar features are observed in the fracture images displayed in **Fig. S3-B(a) - (e)**. The PHf ceramics exhibit a mixture of intergranular and transgranular fractures, while the solid solution ceramics show primarily an intergranular fractural surface. The relative density initially increases and then decreases as the PZnW content

increases, with the highest relative density of 98% achieved in $x = 0.10$, indicating the optimal PZnW content for the densification of the ceramics. The substitution of PZnW significantly promotes grain growth and enhances the relative density, probably due to the presence of some low melting point intermediate and transient phases (Pb_2WO_5, m.p. $= 935$ °C) in addition to the reagents (PbO, m.p. $= 888$ °C) that formed a liquid phase in the $(1-x)$PHf-xPZnW system at high temperatures. The liquid phase can be clearly observed at the grain boundaries in the ceramics of $x \geq 0.10$, as shown in **Fig. S3-B**. The average grain size increases with the increase in PZnW amount, as the liquid phase at the grain boundaries accelerates grain growth. However, a higher PZnW content inhibits grain growth and results in smaller grain sizes. **Fig. S3-C** presents the grain size distribution of the $(1-x)$PHf-xPZnW ceramics with different PZnW contents. The average grain size first increases and then decreases as the x value increases. The ceramics with $x = 0.05$ and 0.10 show a more uniform grain size distribution and dense microstructure, which provide a basis for achieving high energy storage and electric field-induced strain performance under relatively low electric fields.
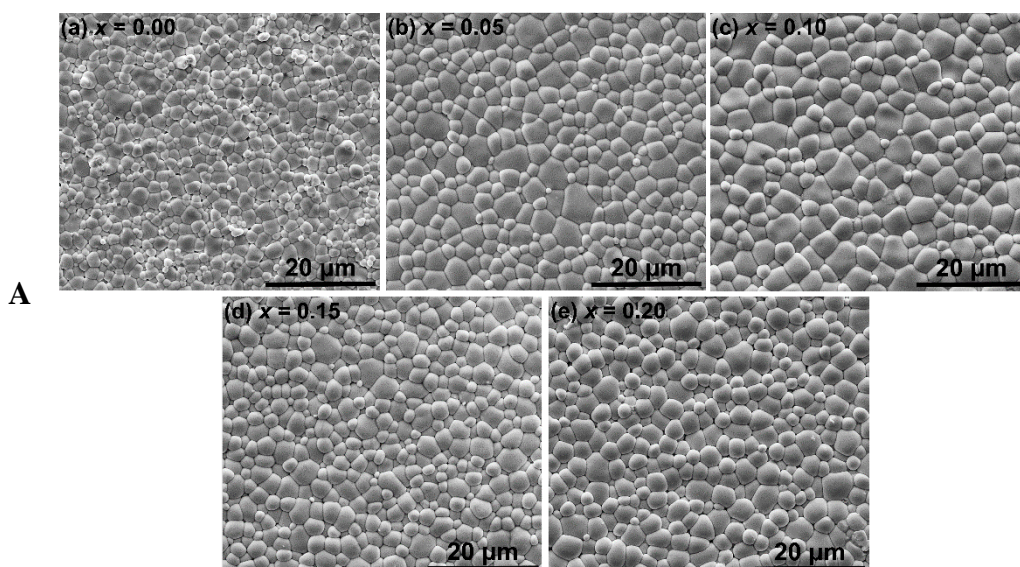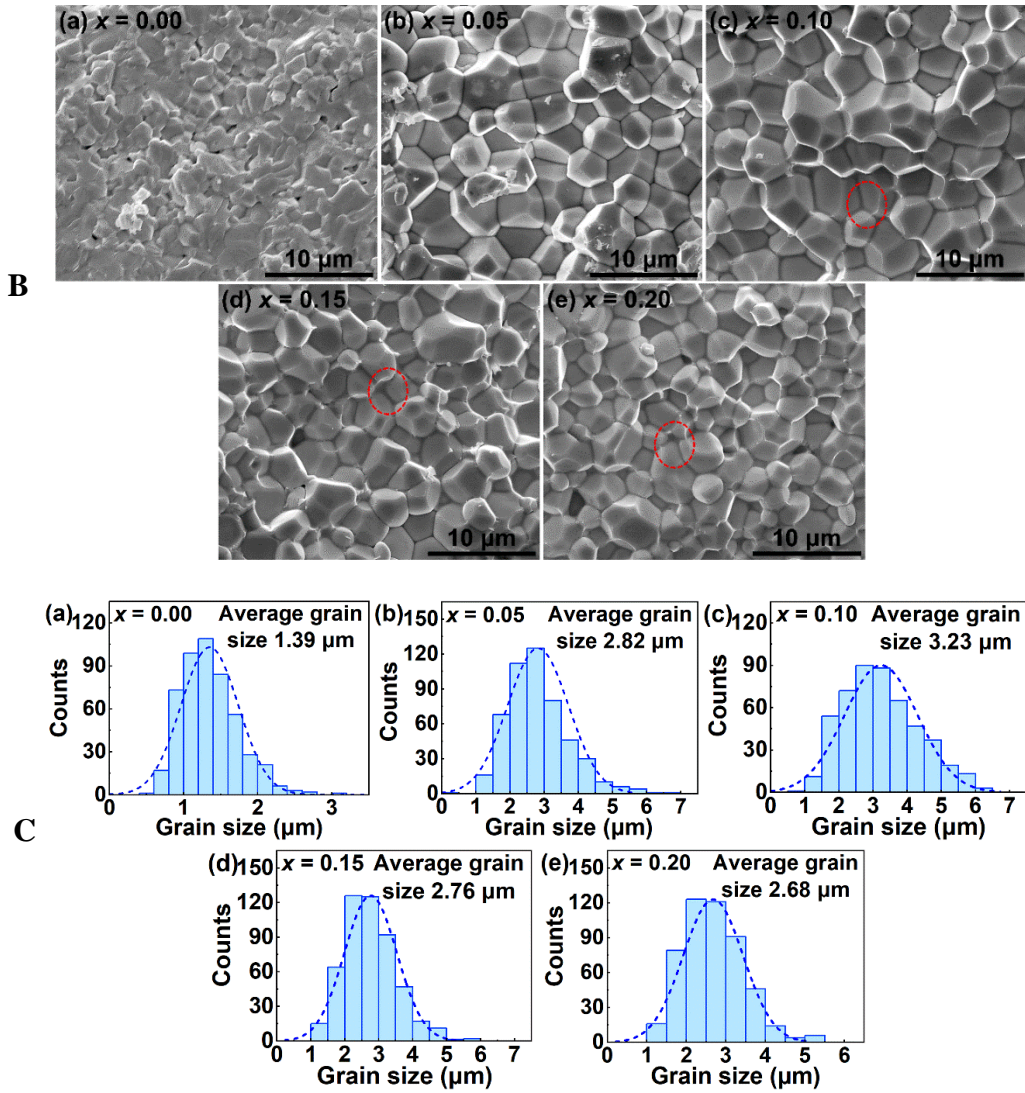
Fig. S3-A. Microstructure of the surfaces of the (1-*x*)PHf-*x*PZnW ceramics with (a) *x* = 0.00, (b) *x* = 0.05, (c) *x* = 0.10, (d) *x* = 0.15, and (e) *x* = 0.20. **Fig. S3-B.** Microstructure of the fractures of the (1-*x*)PHf-*x*PZnW ceramics with (a) *x* = 0.00, (b) *x* = 0.05, (c) *x* = 0.10, (d) *x* = 0.15, and (e) *x* = 0.20. The liquid phases in the grain boundary are marked by the cycles. **Fig. S3-C**. (a)-(e) The average grain size distributions of the (1-*x*)PHf-*x*PZnW ceramics with different PZnW contents.

Fig. S4(a) - (e) illustrates the *P-E* hysteresis loops and the corresponding current versus electric field (*I-E*) curves of the (1-*x*)PHf-*x*PZnW ceramics under ±200 kV/cm (10 Hz) at room temperature. An electric field of ±200 kV/cm is insufficient to induce

the AFE-FE phase transition in the pure PHf ceramic due to its large E_{cr}. As a result, the P-E loop exhibits a linear behavior, and the I-E curves lack significant peaks, leading to a small maximum electric field-induced polarization of ±3.93 $\mu C/cm^2$. This unfavorable outcome hampers energy storage capabilities. In contrast, the $(1\text{-}x)$PHf-xPZnW ceramic samples with $x = 0.05 \sim 0.20$ possess typical double P-E hysteresis loops with a high P_{max} and a low P_r, fully displaying the AFE characteristics.
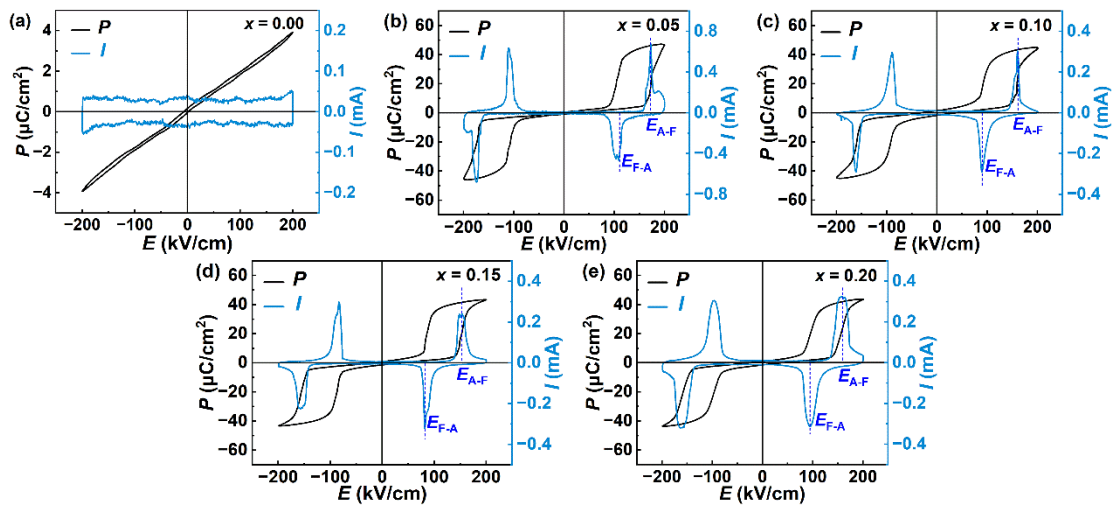

Fig. S4. (a) - (e) P-E loops and the corresponding I-E curves of the $(1\text{-}x)$PHf-xPZnW ceramics measured at 10 Hz.

   Fig. S5 presents the enlarged view of the XRD patterns of the $(1\text{-}x)$PHf-xPZnW ceramics with different PZnW contents. It is observed that the intensity of the $1/4(hkl)_{pc}$ superlattice reflection peaks slightly decreases with the increase of PZnW content. This trend suggests that the substitution of Hf^{4+} by $(Zn_{1/2}W_{1/2})^{4+}$ reduces the driving force for the antiparallel displacement of Pb^{2+} along the $[110]_{pc}$ direction, indicating some degrees of dipole frustration. Additionally, notable changes are observed in a new $1/2(hkl)_{pc}$ superlattice reflection peak at $(3/2,1/2,0)_{pc}$ (marked as red pentagrams) in the $(1\text{-}x)$PHf-xPZnW solid solutions, particularly with a higher PZnW content ($x \geq 0.10$).

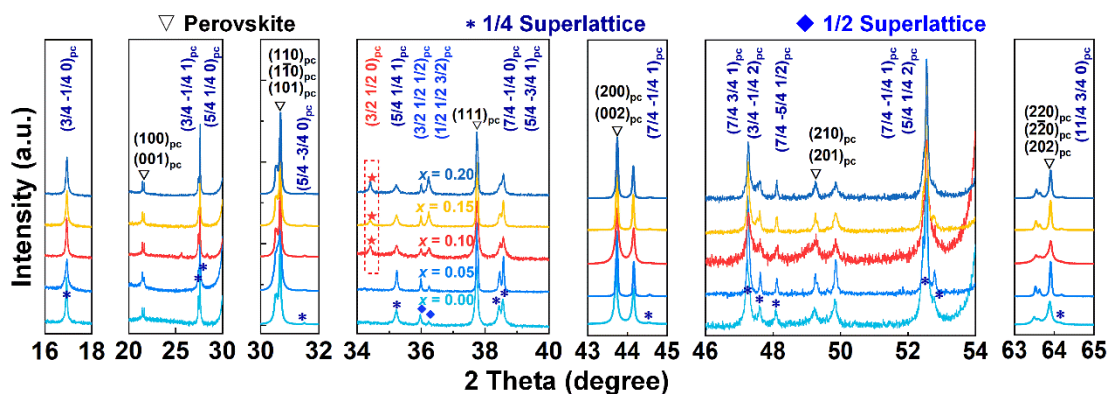These changes suggest the formation of partial chemical ordering on the B site due to the addition of PZnW.

Fig. S5. Enlarged view of the XRD patterns of the (1-*x*)PHf-*x*PZnW ceramics with different PZnW contents at room temperature.

To determine the local structural evolution and the chemical ordering of the (1-*x*)PHf-*x*PZnW ceramics, XRD patterns, and Raman spectra are measured from 10 to 40 degrees and from 50 to 1000 cm^{-1} at RT, respectively. Because of the very low intensities of the diffraction peaks associated with the chemical ordering, the scanning speed in the XRD experiment was set as slow as 3500 s per step. The results are shown in **Fig. S6(a) and (b)**. As shown in **Fig. S5 and Fig. S6(a)**, a new 1/2(*hkl*)$_{pc}$ superlattice reflection peak (marked as red pentagrams) associated with the chemical ordering of B site is obviously observed in the (1-*x*)PHf-*x*PZnW solid solutions with a high PZnW content ($x \geq 0.10$), implying that the substitution of PZnW leads to a partial chemical ordering on the B site. In addition, the Raman spectra of (1-x)PHf-xPZnW ceramics are illustrated in **Fig. S6(b).** The Raman spectra of the (1-*x*)PHf-*x*PZnW solid solution exhibit similarities to that of pure PHf, indicating that the substitution of PZnW does

not change the crystal structure symmetry of PHf in the range of $x = 0.00 \sim 0.20$. Among

the Raman peaks, one marked with the dark-blue arrow at 122 cm^{-1} associated with the

oxygen octahedral tilt vibration exists in all of the composition, and its intensity and

wavenumber do not vary obviously with increasing PZnW content. However,

additional Raman peaks marked by the red arrows at around 842 and 927 cm^{-1} are

activated for the $x = 0.05 \sim 0.20$. These peaks are attributed to the partial chemical

ordering on the B site, resulting from the substitution of the Zn^{2+} and W^{6+} ions for the

Hf^{4+} ion. The intensity of those peaks increases with increasing PZnW content,

indicating that the degree of order is enhanced by the substitution of PZnW for PHf.

Those peaks can be assigned to the stretching of the highly rigid Zn-O-W bonds

consisting, in fact, of a totally symmetric breathing vibration of the oxygen octahedra.

Compared to XRD diffraction, Raman spectroscopy is especially sensitive to small

domains. Therefore, Raman scattering is capable of detecting B-site ordering even in

the composition with low PZnW content, where the B-site ordering domains are too
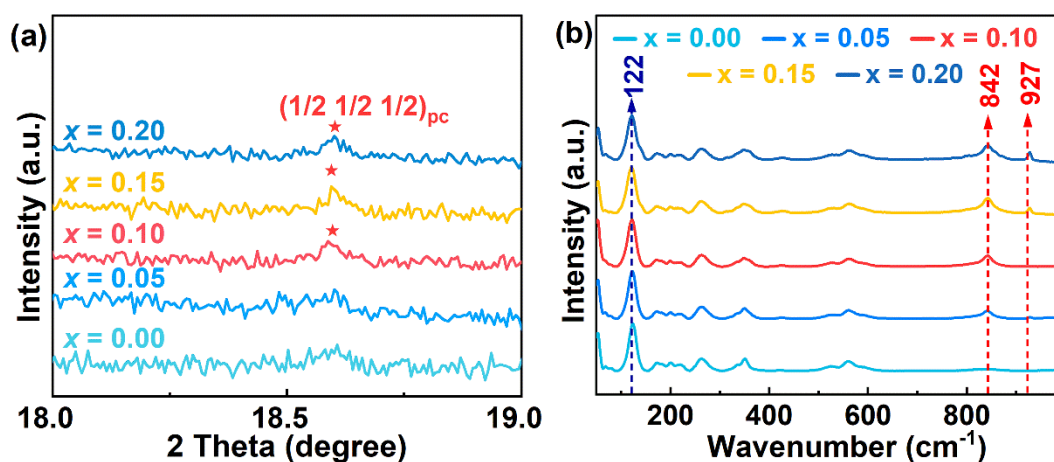
small to be detected by XRD.

Fig. S6. (a) The $(1/2,1/2,1/2)_{pc}$ superlattice reflection peaks of the $(1-x)$PHf-xPZnW solid solutions were revealed by a very slow scan on a laboratory X-ray diffractometer. (b) Room temperature Raman spectra of the $(1-x)$PHf-xPZnW ceramics.

Fig. S7 shows the temperature dependence of the dielectric properties from RT to 300 °C for $(1-x)$PHf-xPZnW ceramics with different compositions upon heating. It is evident that all the ceramic samples exhibit two dielectric peaks, corresponding to the phase transitions from the AFE$_I$ (O$_1$) phase to the AFE$_{II}$ (O$_2$) IM phase, and subsequently to the PE$_C$ phase. Meanwhile, both phase transition temperatures decrease with progressively PZnW content. It is worth mentioning that no obvious frequency dispersion of the maximum dielectric constant is observed for any of the samples, although there is a slight decrease with increasing frequency.
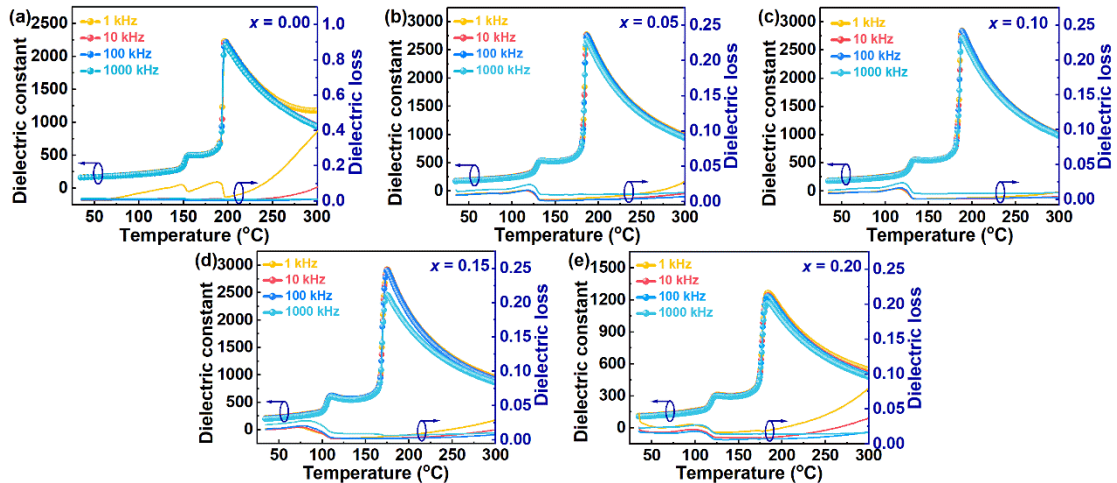

Fig. S7. (a)-(e) Temperature dependence of the dielectric properties of the $(1-x)$PHf-xPZnW ceramics ($x = 0.00$, 0.05, 0.10, 0.15, and 0.20) measured at various frequencies upon heating.

Fig. S8 shows the P-E hysteresis loops of the $(1-x)$PHf-xPZnW ceramics measured at RT, and elevated temperatures of 140, 170, and 210 °C. The measurements were

conducted under an applied electric field of ±100 kV/cm at 10 Hz. All compositions exhibit similar trends with increasing temperature, except for pure PHf, which is due to the higher E_{cr} of PHf. It is noteworthy that the IM phase of all compositions exhibits AFE characteristics.
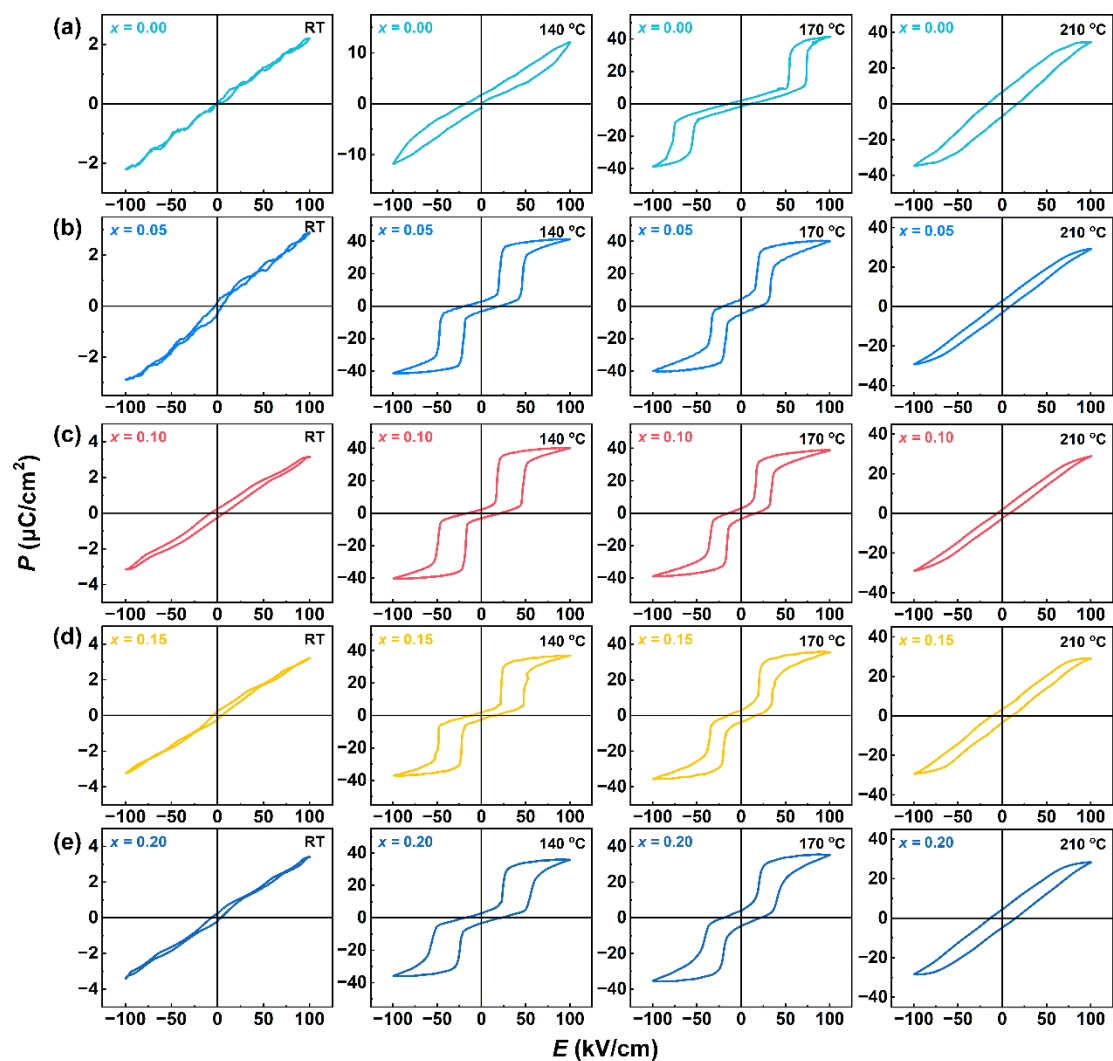

Fig. S8. (a)-(e) *P-E* loops of the (1-*x*)PHf-*x*PZnW ceramics measured at different temperatures under 10 Hz.

Table S2. Lattice parameters in the various phases of the $x = 0.10$ ceramic at different temperatures.

Temperature (ºC)	Space group	Lattice parameters			R-factors		
		a (Å)	b (Å)	c (Å)	R_{wp} (%)	R_{exp} (%)	R_P (%)
25	*Pbam*	5.829553	11.674887	8.178056	4.53	2.45	3.28
80	*Pbam*	5.830140	11.674260	8.181820	5.26	3.51	3.96
130	*Imma*	5.834320	8.200870	5.834180	4.75	2.48	3.38
150	*Imma*	5.834990	8.209995	5.834644	4.69	2.46	3.36
170	*Imma*	5.834581	8.216613	5.834968	4.78	2.45	3.38
190	*Pm$\bar{3}$m*	4.123120	4.123120	4.123120	5.04	2.43	3.50
210	*Pm$\bar{3}$m*	4.123890	4.123890	4.123890	4.67	2.44	3.31